Journal of Marine Systems 77 (2009) 459–472

Contents lists available at ScienceDirect

Journal of Marine Systems

journal homepage: www.elsevier.com/locate/jmarsys

Late summer stratification, internal waves, and turbulence in the Yellow Sea

Zhiyu Liu [a,*], Hao Wei [a], I.D. Lozovatsky [b,c], H.J.S. Fernando [b]

[a] Physical Oceanography Laboratory, Ocean University of China, Qingdao 266100, PR China
[b] Arizona State University, Department of Mechanical and Aerospace Engineering, Center for Environmental Fluid Dynamics, AZ 85287-8909, USA
[c] P.P. Shirshov Institute of Oceanology, Russian Academy of Sciences, Moscow 117997, Russia

ARTICLE INFO

Article history:
Received 24 September 2007
Received in revised form 11 July 2008
Accepted 1 November 2008
Available online 11 November 2008

Keywords:
The Yellow Sea
Turbulence
Soliton

ABSTRACT

Microstructure profiling measurements at two locations in the Yellow Sea (a deeper central basin and a local shelf break) were analyzed focusing on tidal and internal-wave induced turbulence near the bottom and in the pycnocline. A classical three-layer density structure consisting of weakly stratified surface and bottom boundary layers and a narrow sharp pycnocline is developed by the end of warm season. Turbulence in the surface layer was not influenced by the tidal forcing but by the diurnal cycle of buoyancy flux and wind forcing at the sea surface. The enhanced dissipation and diffusivity generated by the shear stress at the seafloor was found in the water interior at heights 10–15 m above the bottom with a phase shift of ~5–6 m/h. No internal waves, turbulence, or mixing were detected in the pycnocline in the central basin, in contrast to the pycnocline near the local shelf break wherein internal waves of various frequencies were observed all the time. The thickness of the surface layer near the local shelf break slightly exceeded that of the bottom layer (20 vs. 18 m). A 5–6 m high vertical displacement of the pycnocline, which emerged during the low tide, was arguably caused by the passage of an internal soliton of elevation. During this episode, the gradient Richardson number decreased below 0.25 due to enhanced vertical shear, leading to local generation of turbulence with dissipation rates exceeding the background level by an order of magnitude.

1. Introduction

The Yellow Sea (YS) is a shallow basin in the northern East China Sea with a mean depth of 44 m. During the warm season from late spring to early autumn, stratification in YS is characterized by a strong thermocline. A tidal front horizontally separates the well-mixed shallow regions from the highly stratified deeper regions occupied by the Yellow Sea Cold Water Mass (YSCWM) beneath the thermocline (e.g., Qiao et al., 2006). By the end of the warm season in late September, distinct 3-layer stratification is developed. Weakly stratified surface and bottom boundary layers are often separated by a sharp, narrow (few meters thick) pycnocline. This stratification closely resembles the idealized modeling scenario that is often assumed in theoretical and laboratory studies of stratified flows (e.g., Turner, 1979; Thorpe, 2005). The microstructure and current measurements in YS in late summer, therefore, are not only valuable in understanding this specific natural environment but also to validate results of numerous theoretical, laboratory, and numerical studies of fundamental importance (e.g., Liu et al., 1998; Strang and Fernando, 2001a,b; Hsu et al., 2000; Fringer and Street, 2003).

In the past three decades, profiling measurements of small-scale shear in aquatic systems have emerged as a major tool for the evaluation of turbulent kinetic energy dissipation rate ε in the ocean (Osborn, 1980). Although direct measurements of ε in the East China Sea (Matsuno et al., 2006; Lee et al., 2006), tidally-energetic European shelf seas (the Irish and North Seas), and shallow shelves (the New England shelf) have been reported (e.g., Simpson et al., 1996; Dickey and Williams III, 2001; Rippeth et al., 2001; Howarth et al., 2002; Rippeth et al., 2003), no such measurements have been conducted in YS hitherto.

* Corresponding author.
E-mail address: zhiyuliu@ouc.edu.cn (Z. Liu).

0924-7963/$ – see front matter © 2008 Elsevier B.V. All rights reserved.
doi:10.1016/j.jmarsys.2008.11.001

In contrast to turbulent mixing in non-stratified shallow waters, which can be well simulated by different turbulence closure models (e.g., Simpson et al., 1996; Baumert and Peters, 2000), mixing in stratified tidally-affected shelf seas is still poorly understood. The bottom turbulence is mainly driven by the tidal vertical shear generated at the seafloor; internal tide and higher-frequency internal waves may generate turbulence inside the stratified water column. The influence of internal tide on the generation of turbulence in shallow-water basins has been reported in several studies (e.g., Holloway et al., 2001; Sharples et al., 2001; Rippeth and Inall, 2002; Rippeth, 2005; Rippeth et al., 2005). The flow oscillations at near-inertial frequencies (inertial oscillations), mostly resulting from wind forcing, produce internal shear, which in turn triggers near-inertial internal waves that propagate almost vertically (e.g., van Haren, 2000; Rippeth and Inall, 2002; MacKinnon and Gregg, 2003; Rippeth, 2005; Rippeth et al., 2005). The effect of near-inertial waves on the generation of sheared turbulence in the pycnocline is particularly important in seas such as the Mediterranean Sea and the Black Sea (Lozovatsky and Fernando, 2002), where tidal currents are weak. In tidally energetic seas, however, near-inertial oscillations could be quickly damped by tidal currents through enhanced bottom friction (J.H. Simpson, personal communication). In inner-shelf seas away from the shelf break and abrupt topography, degeneration of higher frequency internal waves is a major source of internal mixing in the absence of strong winds.

The microstructure measurements carried out with a TurboMap profiler (Wolk et al., 2002) in two shallow regions of the East China Sea were recently reported by Matsuno et al. (2006) and Lee et al. (2006). One region was at the outer northeastern shelf of the East China Sea south of 30.5°N (Matsuno et al., 2006) and the other was southeast of the Cheju Island (~32°N, 125°E; Lee et al., 2006). In July 2003 and 2004, Matsuno et al. (2006) observed $\varepsilon > 10^{-7}$ W/kg near the seafloor and in the surface layer, whereas $\varepsilon < 10^{-8}$ W/kg was observed below the Changjiang Diluted Water (e.g., Chang and Isobe, 2003). Lee et al. (2006) reported the highest level of the dissipation ($\varepsilon > 10^{-6}$ W/kg) in the surface turbulent layer with enhanced dissipations corresponding to low salinity surface lenses. Below the surface layer, intermittent patches of turbulence ($\varepsilon > 10^{-7}$ W/kg) were detected within the seasonal pycnocline as well as close to the bottom. The lowest level of ε ($< 10^{-9}$ W/kg) was found within the water column below the pycnocline, at depths associated with the Tsushima Warm Current Water (e.g., Lie and Cho, 1994). The measurements taken in August 2005 depicted an approximately 3-layer summer stratification, consisting of nearly isothermal 10–20 m upper layer separated from the lower weakly-stratified layer by a relatively thick (~10 m) pycnocline. Tidal-induced variations of ε, however, were not discussed by Matsuno et al. (2006) and Lee et al. (2006) because of relatively short time of their microstructure measurements at a given location.

A distinct tidal cycle of ε variability was reported by Lozovatsky et al. (2008a,b) based on *in situ* ADV (acoustic Doppler velocimeter) measurements in the bottom boundary layer (BBL) of YS. The measurements were conducted in 2005 during the cold season (in March and December) when the whole water column was well mixed (Liu and Wei, 2007).

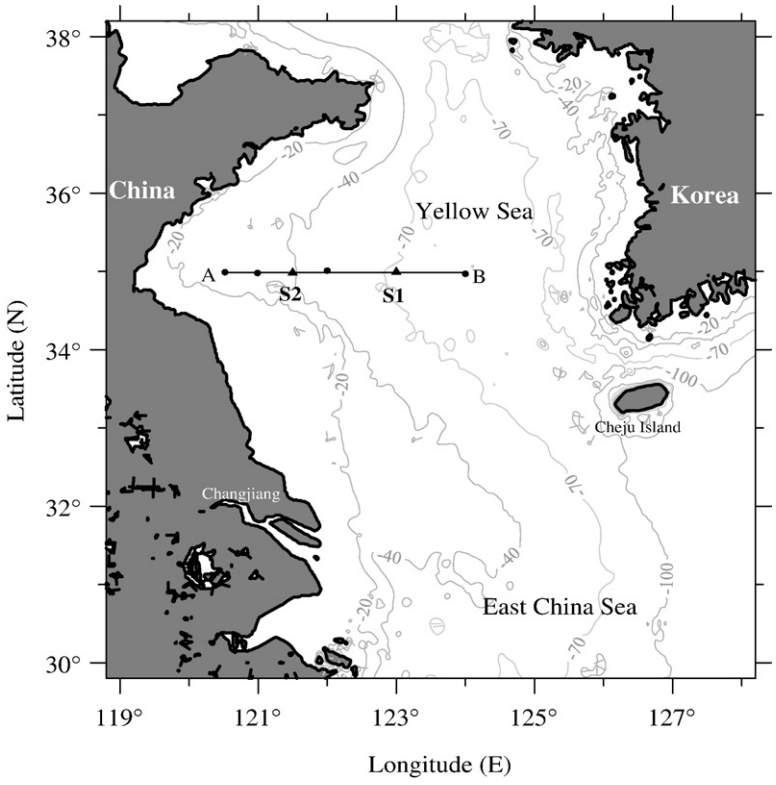

Fig. 1. Bathymetry of the Yellow Sea and adjacent regions. The MSS-60 microstructure measurements were conducted at **S1** and **S2**. CTD stations are shown by dots. The ADCP data were collected at **S2**. Bathymetric contours are in meters.

Local processes, such as seiching and near-bottom convection were found to influence ε near the seafloor. The authors reported high dissipation rate evaluated via the inertial subrange of the ADV velocity spectra (e.g., Kim et al., 2000; Lozovatsky et al., 2008b), which sometimes exceeded 10^{-5} W/kg in the well-mixed tidal BBL. The influence of strong summer stratification on vertical mixing in YS is still unknown. To this end, we carried out a field campaign in September 2006, at the closing stage of the warm season, which included a CTD transect and a series of microstructure profiles and ADCP mooring measurements at two anchored stations. The aim was to map and compare the vertical distribution of ε and the eddy diffusivity K_N in relatively deep central basin of YS (the mean depth $H_B = 73$ m) and near a shallow local shelf break ($H_B = 38$ m). The study was focused on the influence of tidal currents and internal waves on the evolution of stratification and turbulence in the thermocline and tidal BBL of YS. It is not feasible, however, to investigate such low frequency processes as inertial oscillations given the short duration of the measurements (25 h), which only slightly exceeded the inertial period at the sites (20.9 h). Instrumentations, observational setup and principal steps of data processing are described in Section 2. Results and discussion are presented in Section 3, and a summary is given in Section 4.

2. Instrumentations, observations, and data processing

The measurements were carried out in central YS during September 19–26, 2006 onboard of the R/V Beidou. Six hydrographic stations were taken along a transect (Fig. 1) using a Seabird SBE-25 CTD profiler. Multiple casts of a tethered microstructure profiler MSS-60 (Prandke and Stips, 1998) were launched from the sea surface down to the bottom at two stations **S1** (September 20–21, $\varphi = 35.01°$N, $\lambda = 123.00°$E; the mean depth $H_B = 73$ m) and **S2** (September 25–26, $\varphi = 35.00°$N, $\lambda = 121.50°$E; $H_B = 38$ m) over two semidiurnal tidal cycles (25 h). The hourly launches of MSS-60 consisted of 3 consecutive casts to make the burst-averaged data statistically robust. The interval between individual casts was 4–5 min at **S1** and 2–3 min at **S2**. The microstructure profiler carried two parallel airfoil (PNS98) sensors, a fast-response temperature sensor (FP07), three standard CTD sensors and an accelerometer. The sampling rate for all sensors was 1024 Hz, thus enabling the measurement of small-scale shear with a vertical resolution of ~6 mm for a typical falling speed of the profiler of ~0.65 m/s.

An upward-looking 600 kHz RDI ADCP was mounted on the seafloor at **S2**, allowing continuous measurements of along-beam velocities with a ping rate of 2 Hz. The data were ensemble averaged over 2 s (i.e. four pings) before recording. The ADCP profiles of zonal $u(\zeta)$ and meridional $v(\zeta)$ components were obtained only in the lower 20 m of the water column, at heights of $\zeta = 2.4$–20.4 m above the bottom (mab) with a vertical interval $\Delta\zeta = 0.75$ m. Campbell Scientific package CR1000 was used for standard meteorological observations.

The processing of MSS-60 data followed recommendations of Stips and Prandke (2000), Stips (2005) and Roget et al. (2006). High-amplitude spikes in all signals were detected and removed using an iterative procedure. The low frequency

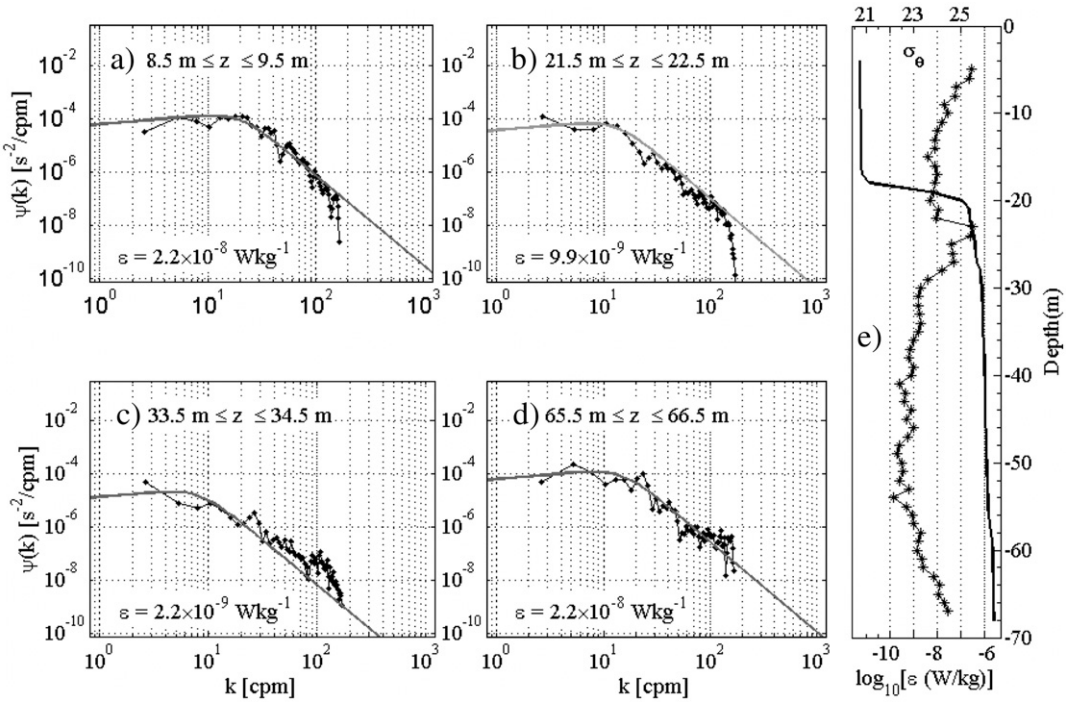

Fig. 2. Examples of the shear spectra at **S1** for the surface layer (a), pycnocline (b), below the pycnocline (c), and near the seafloor (d). The estimates of the dissipation rate ε for the specified depth ranges as well as the best fits to the Nasmyth (1970) spectrum are shown in (a–d); corresponding $\varepsilon(z)$ and $\sigma_\theta(z)$ profiles are in panel (e).

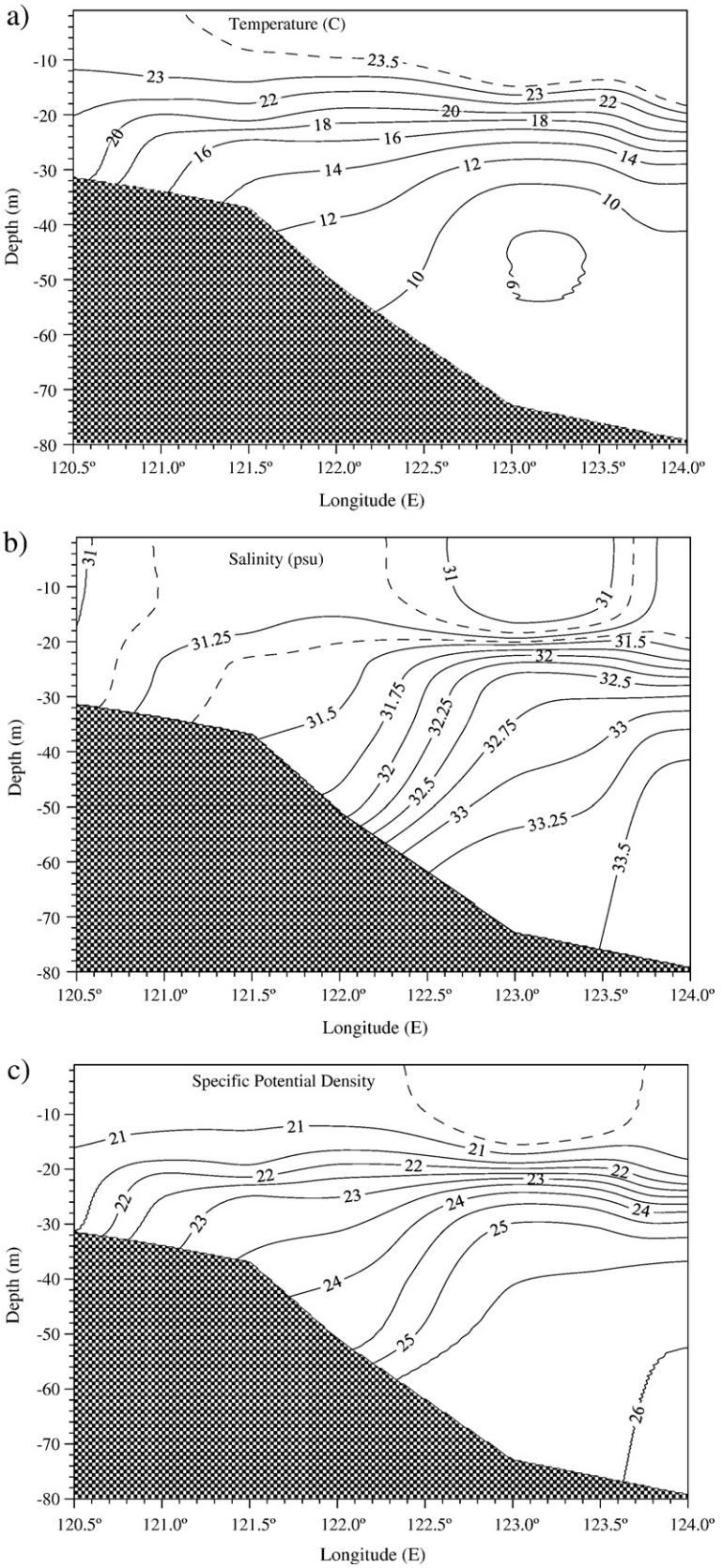

Fig. 3. Temperature (a), salinity (b), and specific potential density (c) contour plots along the section AB (see Fig. 1).

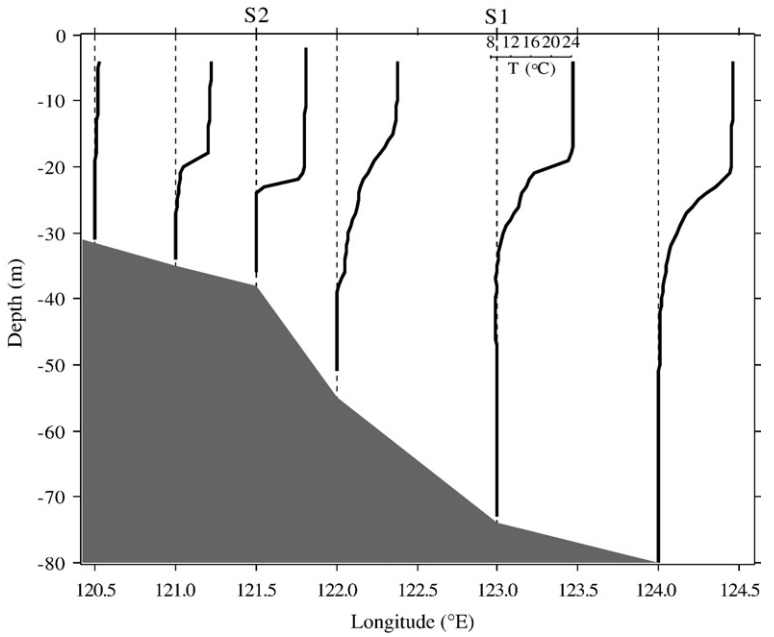

Fig. 4. Temperature profiles at the stations of the section **AB** plotted over the bathymetry. The same temperature scale was used for all profiles; the station locations are shown by the dashed lines.

variations of shear signal and high frequency noise were then removed by a second order Butterworth band-pass filter with cut-off frequencies 1 and 100 Hz, corresponding to the wavenumbers $k = 1.5$ and 308 cpm, respectively.

The turbulent dissipation rate was evaluated from the small-scale shear signal using the isotropic turbulence formula

$$\varepsilon = 7.5\nu\overline{(\partial u'/\partial z)^2} \quad (1)$$

where the dependence of molecular viscosity of the seawater ν on temperature (strong), salinity and pressure (weak) was accounted for using the Matlab scripts of the Seawater toolbox (ftp://ftp.marine.csiro.au/pub/morgan/seawater). The variances in Eq. (1) were calculated by integrating the small-scale shear spectra computed at 1-m depth intervals over 2 cpm$<k<k_K$, where $k_K = (\varepsilon/\nu^3)^{1/4}/2\pi$ is the Kolmogorov wavenumber. Because k_K is a function of ε, an iterative procedure was used to calculate the shear variance, and thus ε (Stips and Prandke, 2000). Several examples of the shear spectra and corresponding estimates of the dissipation rate are given in Fig. 2. In the surface and bottom boundary layers, the spectra befittingly follows the Nasmyth spectrum (Nasmyth, 1970), which is considered a benchmark for shear spectra in the inertial-viscous subrange of small-scale turbulence (e.g., Thorpe, 2005) along with the Panchev and Kesich (1969) modeling spectrum (Roget et al., 2006).

The vertical eddy diffusivity K_N was calculated using the Osborn (1980) formula

$$K_N = \gamma\frac{\varepsilon}{N^2} \quad (2)$$

where the squared buoyancy frequency N^2 was estimated at the same 1-m segments of the smoothed (reordered) potential density profiles as those were used for ε. Here we employed traditional constant value of mixing efficiency $\gamma = 0.2$ although a Richardson-number-dependent γ has also been proposed in several studies (e.g., Lozovatsky et al., 2006).

3. Results and discussion

3.1. Thermohaline structure

The contour plots of temperature T, salinity S, and specific potential density σ_θ along the section **AB** (see Fig. 1) are shown in Fig. 3. This hydrographic section (between 35.0°N, 120.5°E and 35.0°N, 124.0°E) encompassed sites **S1** and **S2**. The three-layer stratification in YS typical for the late summer is evident. Warm ($T = 22$–23 °C) well-mixed layer occupied ~20 upper meters of the water column. In the thermocline, $z = -20$ to -32 m, the temperature decreased from 23.5 to ~10 °C. Below the thermocline, a bulk of cold water with the lowest temperature ($T<9$ °C) centered near the longitude $\lambda = 123.2$°E was observed (Fig. 3a).

The salinity in the deepest part of section **AB** increased from 31.1 psu at the surface to 33.7 psu near the seafloor (Fig. 3b). The upper layer contained a low-salinity lens centered at $\lambda = 123.2$°E. Coastal surface waters of low salinity ($S<31$ psu) were also evident at the western edge of the section. The halocline ($31.25<S<32.5$ psu) generally coincided with the thermocline along **AB**. Below the halocline, salinity gradually increased with depth from 32.5 to 33.7 psu.

The contours of the specific potential density σ_θ (Fig. 3c) suggest an along-slope quasi-geostrophic flow in the western, shallower part of the section. The mean tidal residuals in the water interior at **S2** calculated for two semidiurnal periods of ADCP measurements were estimated as $<u_{res}> = -0.3$ cm/s and $<v_{res}> = -4.6$ cm/s, indicating the existence of an along-

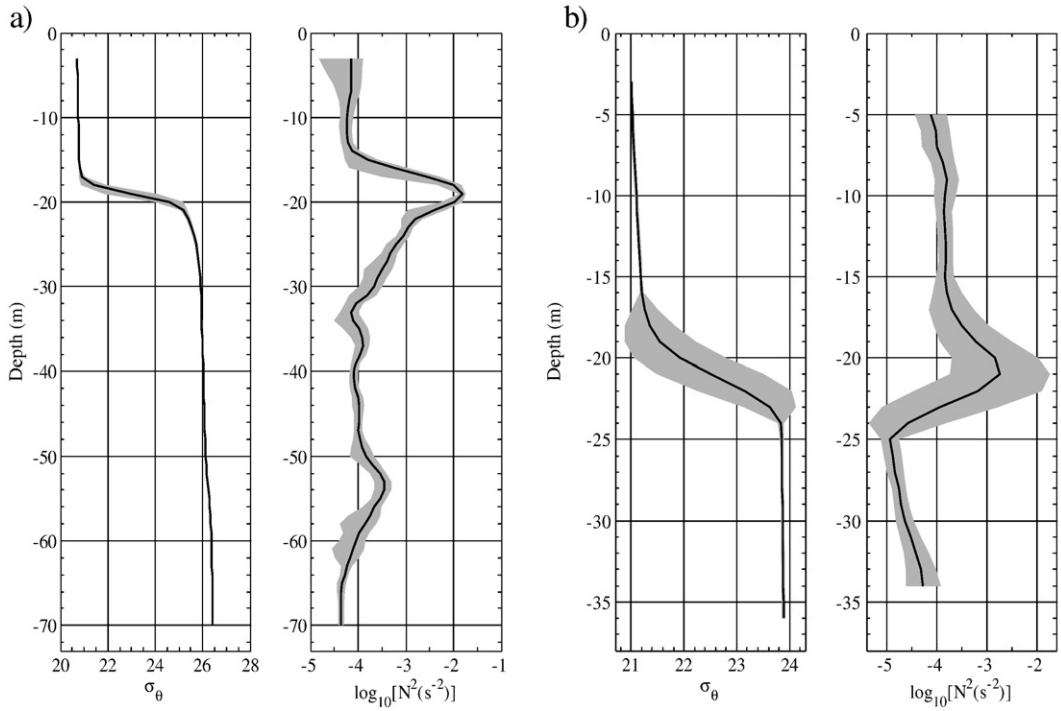

Fig. 5. The ensemble averaged profiles over two tidal cycles of specific potential density $\hat{\sigma}_\theta(z)$ and the logarithm of squared buoyancy frequency $log_{10}\hat{N}^2(z)$ at **S1** (a) and **S2** (b). The mean ± standard deviation ranges are shaded.

shelf current, which could be associated with the Yellow Sea Coastal Current. This cold southward directed perennial flow dominated the circulation on the northwestern shelf of the southern YS.

The contour plots in Fig. 3 do not show a narrow thermocline and pycnocline over the local shelf break due to the nature of the gridding procedure used, which accounts for a substantial difference between the vertical and horizontal resolutions of the CTD data at the transect. The typical aspect ratio between the horizontal and vertical scales of thermohaline features of oceans rarely exceeds 10^3 (Fedorov, 1978). Therefore, the vertical gridding of several meters are appropriate to represent the characteristic mean thermohaline structure for stations separated by several tens of kilometers at section **AB**, but such grid sizes are not suitable for presenting the details of stratification. To better illustrate the thermocline thickness variations along the **AB** transect, temperature profiles at the stations of the section are shown in Fig. 4 over the bathymetry. A remarkable sharpening of the thermocline over the local shelf break could be related to the enhancement of topographically induced turbulence, which almost completely mixed the bottom boundary layer up to ~15 m above the seafloor. Possible transformation of a relatively wide thermocline, which was observed east of the local shelf break (Fig. 4), to a narrow one at the break and further onshore could also be associated with packets of nonlinear internal waves generated at the break due to the interaction between internal tide and topography. Navrotsky

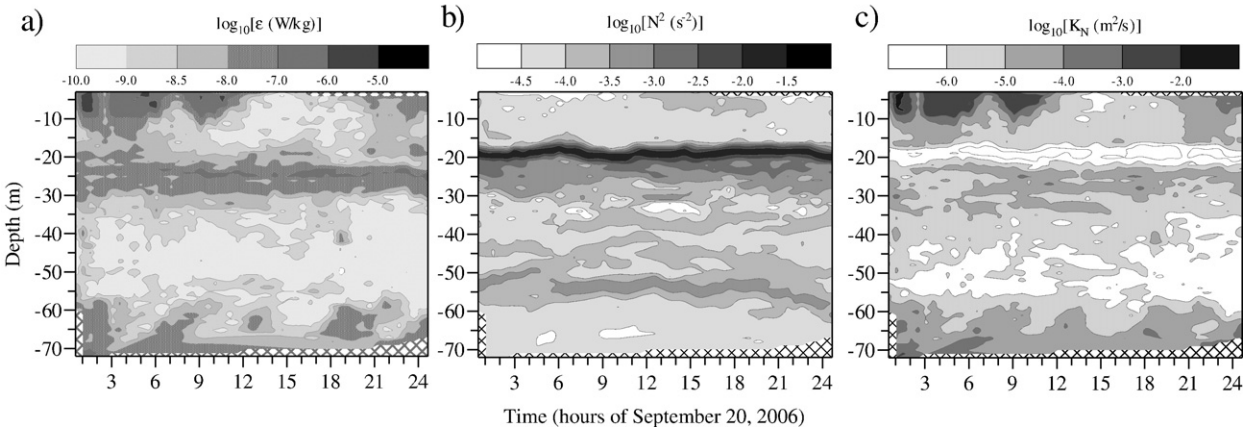

Fig. 6. The time-depth variations of the logarithm of turbulent kinetic energy dissipation rate (a), squared buoyancy frequency (b), and eddy diffusivity (c) at **S1**.

et al. (2004) showed that this process may trigger internal mixing within a wide pycnocline, thus splitting it into two narrow interfaces. If this actually happens, then a plausible scenario is the erosion of upper interface by surface mixing (it can still be traced at $z\sim-15$ m), and subsequent evolution of the splitting thermocline/pycnocline into the observed temperature/density structure with one sharp thermocline/pycnocline over the shelf at $z=-20$ to -22 m.

The stratification at **S1** and **S2** during two tidal cycles is specified by the ensemble-averaged profiles of $\hat{\sigma}_\theta(z)$ and $log_{10}\hat{N}^2(z)$ shown in Fig. 5. At **S1**, the upper 16-m layer was linearly stratified with a relatively low $N^2=(4\text{–}8)\times10^{-5}\,s^{-2}$. In the narrow pycnocline, $z=-17$ to -22 m, the buoyancy frequency reached maximum $N^2_{max}=2\times10^{-2}\ s^{-2}$ at $z=-19$ m. The layer between the pycnocline base and $z=-50$ m was weakly stratified with nearly constant $N^2=9\times10^{-5}\ s^{-2}$. In the depth range -50 to -58 m, the $\hat{\sigma}_\theta(z)$ and $log_{10}\hat{N}^2(z)$ profiles in Fig. 5a exhibit a secondary pycnocline with a maximum $N^2_{max}=3.6\times10^{-4}$ at $z=-54$ m, where the stable density gradient was governed by stable salinity but unstable temperature gradients. A characteristic density ratio across this layer is $R_\rho=\beta S_z/\alpha T_z=4.8$, suggesting a possibility of double-diffusive convection (Kelley et al., 2003). Here the salinity S_z and temperature T_z gradients are 0.035 psu/m and 0.036 C/m, respectively, and the ratio between the salinity contraction and temperature expansion coefficients is $\beta/\alpha=4.95$ C/psu. This double-diffusion favorable layer (see it is also around $z=-60$ m in Fig. 6 of Shi and Wei (2007)) resulted from the interaction between YSCWM and the Yellow Sea Warm Current (YSWC). Note that YSWC originates in the East China Sea as a branch of Kuroshio transporting warm saline water to YS along the central trough, thus influencing a deeper eastern periphery of **AB**. Below the secondary pycnocline, the bottom boundary layer was weakly stratified with the buoyancy frequency changing from $N^2\approx4\times10^{-5}\ s^{-2}$ to almost zero depending on the phase of barotropic tide.

The upper quasi-homogeneous boundary layer at **S2** was only slightly thicker than the bottom boundary layer ($H_{sf}\sim17$ m and $H_{bt}\sim14$ m in the ensemble-averaged density profile $\hat{\sigma}_\theta(z)$). The specific thermohaline structure observed in shallow waters of YS in late summer is a result of solar heating and wind-induced mixing at the sea surface, permanent advection of cold bottom water as well as tidal mixing in the lower part of the water column. The mean buoyancy frequency in the upper layer ($\overline{N}^2_{sf}=(1\text{–}2)\times10^{-4}\ s^{-2}$) was substantially larger than that in BBL, where $\overline{N}^2_{bt}=(3\text{–}5)\times10^{-5}\,s^{-2}$. A narrow sharp pycnocline (usually ~2–3 m thick in individual density profiles) separated these two boundary layers. The ensemble averaged profiles of $\hat{\sigma}_\theta(z)$ and $log_{10}\hat{N}^2(z)$ in Fig. 5b exhibit relatively large scatter of the pycnocline position ($\Delta z\approx18\text{–}24$ m), caused mainly by vertical displacements of internal waves of various frequencies. In the pycnocline core ($z=-21$ m), $\overline{N}^2_{pc}=1.5\times10^{-3}\,s^{-2}$ and the lower and upper boundaries of the mean $\pm$ standard deviation are $\sim2\times10^{-4}$ and $\sim1.2\times10^{-2}\ s^{-2}$, respectively. Such high variability of buoyancy frequency at a given depth in the pycnocline at **S2** was induced by internal waves in contrast to the low internal-wave activity observed earlier at **S1**. Below, we discuss in detail the variability of stratification and its influence on turbulence in YS.

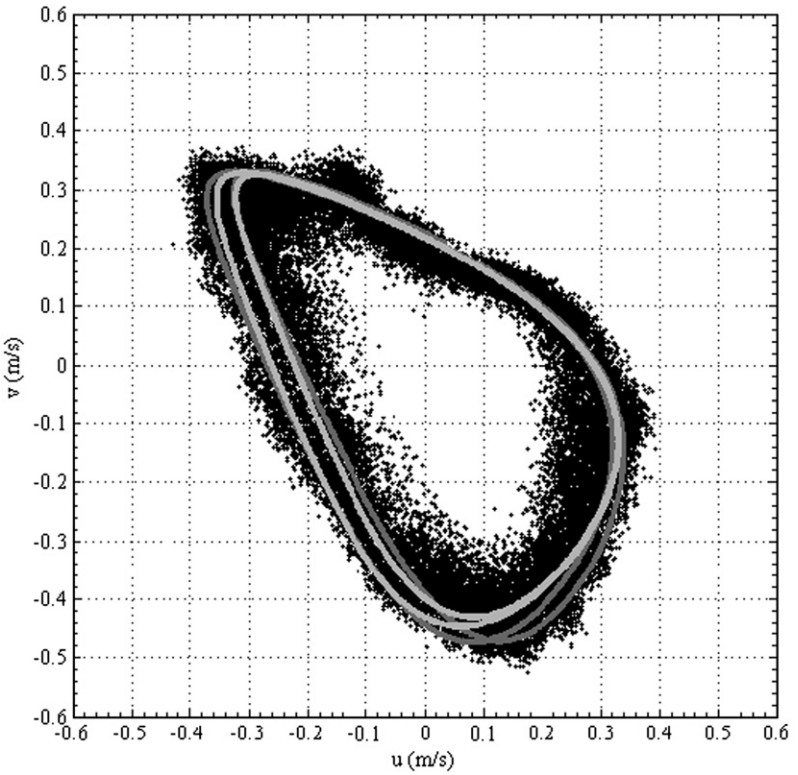

Fig. 7. A hodograph of currents at all ADCP levels at **S2** in the range $\zeta=2.4\text{–}19.6$ mab. Two cycles of tidal ellipses at the lower ($\zeta=15.9$ mab) and upper ($\zeta=19.6$ mab) boundaries of the pycnocline are shown by dark and light grey lines, respectively.

3.2. Time-depth variations of ε, K_N, and Ri

In the absence of episodic storms, semidiurnal M_2 tidal currents are the most powerful dynamic component in nearly all regions of YS. Being a part of the East China Sea, YS is thought to be one of the principal regions of the dissipation of tidal energy (e.g., Egbert and Ray, 2000). Toward the end of the warm season, a combination of strong stratification, permanent tidal forcing and episodic high winds creates favorable conditions for the generation of high-amplitude internal waves. Trains of internal waves have been measured *in situ* (Lee et al., 2006), observed in SAR images (Hsu et al., 2000) and detected by optical sensors of the SPOT satellite (Alpers et al., 2005). The energy sources of turbulence in YS could be mainly attributed to the tidal bottom shear stress, surface wind forcing and breaking and/or degeneration of internal waves.

3.2.1. Central basin – Station S1

The time-depth variations of ε, N^2, and K_N at **S1** are shown in Fig. 6. High values of $\log_{10}\varepsilon$ were found near the sea surface, near the bottom, and just below the pycnocline (Fig. 6a). Strong turbulence ($\log_{10}\varepsilon > -6.5$ [ε is in W/kg]) in the upper 10 m observed between $t=0$ and 9 h was due to a combination of wind forcing (wind speed $W_a=4.4$ m/s; friction velocity $u_{*ss}=0.5$ cm/s) and nighttime convection (buoyancy flux $J_b=9.8\times10^{-8}$ W/kg; note the measurements started at midnight of September 20, $t=0$). Daytime solar radiation and weakening winds ($W_a=2$ m/s) impede the generation of surface turbulence during the afternoon to early evening ($t=12$–20 h), and therefore the dissipation level in the whole upper 20-m layer dropped to a background value ($<10^{-9}$ W/kg). After the sunset, upon initiation of nighttime cooling and convection ($t>21$ h), ε quickly rises to ~10^{-7} W/kg almost across the entire surface layer. The variations of $N^2(z,t)$ across the surface layer are highly correlated with the variations of $\varepsilon(z,t)$; the periods of relatively low ($t=0$–10 and $t>21$ h) and high ($t=12$–20 h) $N^2(z)$ are well matched with the periods of high and low dissipation, respectively (compare Fig. 6a and b). Parameterization of turbulence caused by the combined effects of winds and nighttime convection has been proposed by Lombardo and Gregg (1989) and in a modified form by Lozovatsky et al. (2005), but during the measurements at **S1** and **S2** mean stratification in the upper layer remained weakly stable ($\hat{N}^2 \sim 10^{-5}$ s^{-2}) even at night, and therefore Eq. (2) is still suitable for estimating the eddy diffusivity K_N for the entire observational period. The diffusivity K_N (Fig. 6c) was as high as 10^{-3}–10^{-2} m^2/s during the nighttime, but it rapidly decreased to 10^{-5}–10^{-6} m^2/s in midday because of the restratification, daytime warming and low wind stress. The weakest mixing (lowest K_N) was observed in the sharp pycnocline, $z\approx-18$ to -25 m (Fig. 6c). Under these conditions, Eq. (2) gives values close to the molecular diffusivity $K_N \sim 10^{-7}$ m^2/s, and thus the assumption of $\gamma=0.2$, which is the basis of Eq. (2), may not hold (e.g., Lozovatsky et al., 2006). This is specifically true if there is no source of relatively strong shear that can support turbulence in highly stratified layers. At **S1**, the position of the pycnocline was almost flat (Fig. 6b), indicating low amplitudes of tidal internal waves. The data do not allow analysis of internal waves of higher frequency, but it is safe to assume that even if such waves did exist, they were too feeble to produce substantial vertical mixing. The latter may impede vertical exchange of bio-chemical properties between the upper and lower layers at **S1**. This situation is quite unusual for a dynamically active, tidally-affected region, and it appears that a combination of weak atmospheric forcing, high

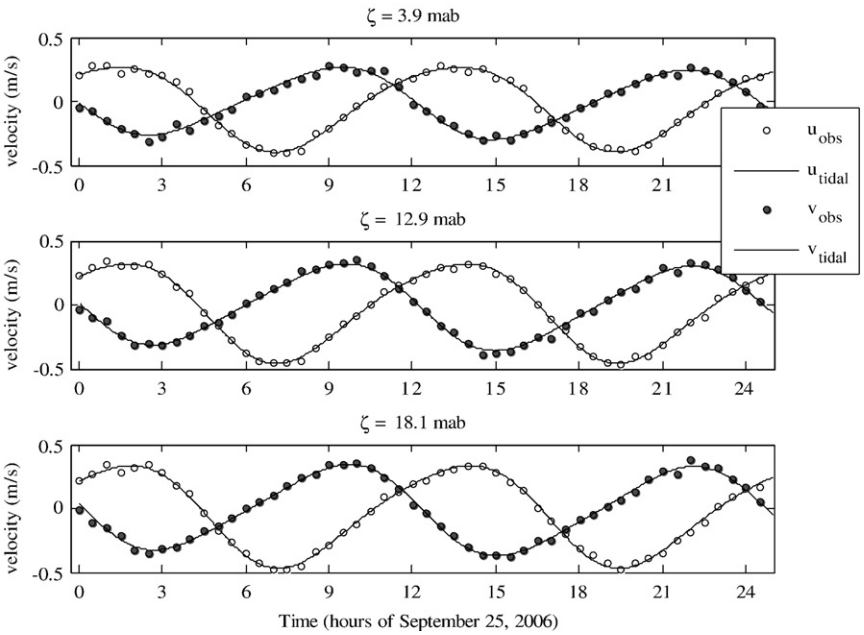

Fig. 8. Temporal variations of unfiltered current components (u_{obs} and v_{obs}) and corresponding tidal components (u_{tidal} and v_{tidal}) at three representative heights: near the seafloor ($\zeta=3.9$ mab, upper panel), in the bottom boundary layer ($\zeta=12.9$ mab, middle panel) and in the vicinity of the pycnocline ($\zeta=18.1$ mab, lower panel). Owing to space constraints, only every thirtieth unfiltered (1 min averaged) current data point is shown in the plots.

stratification and low internal-wave activity prevented vertical exchange across the pycnocline. Note that local generation of internal tides in the region is not feasible due to almost flat bathymetry.

The relatively high dissipation 3×10^{-8}–2×10^{-7} W/kg associated with the diffusivity K_N of ~10^{-5}–10^{-4} m^2/s for $N^2=(8–16)\times10^{-4}$ s^{-2} occurred in a 6–7 m layer just below the pycnocline (compare Fig. 6a and b). The enhancement of therein can arguably be associated with the propagation of internal solitons of depression that appeared at the lower boundary of the pycnocline. They affect the underlying layers for a distance comparable to the amplitude of the soliton. A similar phenomenon was observed in microstructure and ADCP measurements reported by Lee et al. (2006) who noted solitons of depression in the northern part of the East China Sea with amplitudes of 6–7 m. The enhanced dissipation underneath the pycnocline was also reported by van Haren et al. (1999) in the North Sea and Rippeth (2005) in the Irish Sea.

A distinct tidal BBL with strong turbulence (high dissipation) and intense mixing at **S1** extended up to 12–14 mab into the water interior. The dissipation and diffusivity exhibited quarter-diurnal variations with a time lag at various heights from the bottom (Fig. 6a,c). In the absence of velocity measurements at **S1**, however, it is not possible to comment on the turbulence generation mechanisms at this station.

3.2.2. Local shelf break – Station S2

Microstructure and current measurements at the shallower station **S2** near a local shelf break (see Figs. 1 and 4) started on September 25, within five days after completion **S1**. The ADCP data were recorded for 25 h in parallel with a series of MSS-60 casts, allowing the analysis of mixing and turbulence at **S2** in more detail. The dominance of tidal currents at all levels of ADCP measurements at **S2** ($\zeta=2.4$–19.6 mab) is evident from Fig. 7, where unfiltered (1 min averaged) current components u and v show an asymmetric, irregular tidal ellipse with an approximate main axis in NNW–SSE direction. Two cycles of rotation of barotropic tidal currents at the lower and upper boundaries of the pycnocline are also shown in Fig. 7. The barotropic tidal current included all 6 major tidal constituents for YS. The asymmetry of tidal ellipses led to irregular increase/decrease of the shear stresses near the bottom with a quarter-diurnal cycle, which, in turn, affected the intervals where high and low turbulence intensities appear at various heights. The dominance of tidal current is also evident in Fig. 8, where temporal variations of the unfiltered current components (u and v) and corresponding tidal components (u_{tidal} and v_{tidal}) are shown at three representative heights: near the seafloor ($\zeta=3.9$ mab), in the bottom boundary layer ($\zeta=12.9$ mab) and in the vicinity of the pycnocline ($\zeta=18.1$ mab). No inertial oscillations or other types of low frequency variations were registered during the observational period.

Fig. 9 shows the time-depth variations of ε, N^2, and K_N for **S2,** similar to those shown in Fig. 6 for **S1**. In addition, the contours of the vertical shear $Sh(z)=((du/dz)^2+dv/dz)^2)^{1/2}$ overlay the dissipation panel (Fig. 9a). The shear components were calculated using smoothed components of ADCP velocity $\bar{u}$ and $\bar{v}$ after applying the second order Butterworth low-pass filter with a cut-off wavenumber $k_{lp}=0.13$ cpm ($k_{lp}=0.2k_N$, where $k_N=(2\Delta z)^{-1}$ is the Nyquist wavenumber, $\Delta z=0.75$ m). Only a few episodes of enhanced dissipation ($\varepsilon>10^{-7}$ W/kg) can be detected in the upper layer near the sea surface (Fig. 9a), which were induced by short wind bursts. In contrast to **S1**, near-surface turbulence does not show clear diurnal cycle. The stratification in the upper layer (Fig. 9b) was almost unaffected by turbulence ($N^2=(1–2)\times10^{-4}$ s^{-2}). Vertical mixing away from the sea surface was very weak, with K_N~10^{-6} m^2/s, rising to 10^{-5}–10^{-4} m^2/s near the surface (Fig. 9c).

The pycnocline at **S2** was as strong as that at **S1** ($N^2>0.02$ s^{-2}) but narrower (only 2–3 m), and it was affected by tidal internal waves (Fig. 9b). The mean magnitude of vertical pycnocline displacement was ~4 m over a period of ~6 h. A hint of semidiurnal cycle evident from the pycnocline displacements suggests a wide spectrum of internal oscillations influenced not only by the tidal internal waves but also waves of higher frequencies. The energy-preserving frequency spectra $fE_{U_r}(f)=0.5[fE_{U_r}+fE_{v_r}]$ of horizontal tidal residuals u_r and v_r indeed shows several statistically confident maxima (Fig. 10) that indicate quasi-sinusoidal internal waves with periods of ~43, 18, 14, and 11 min. The most energetic maxima were observed

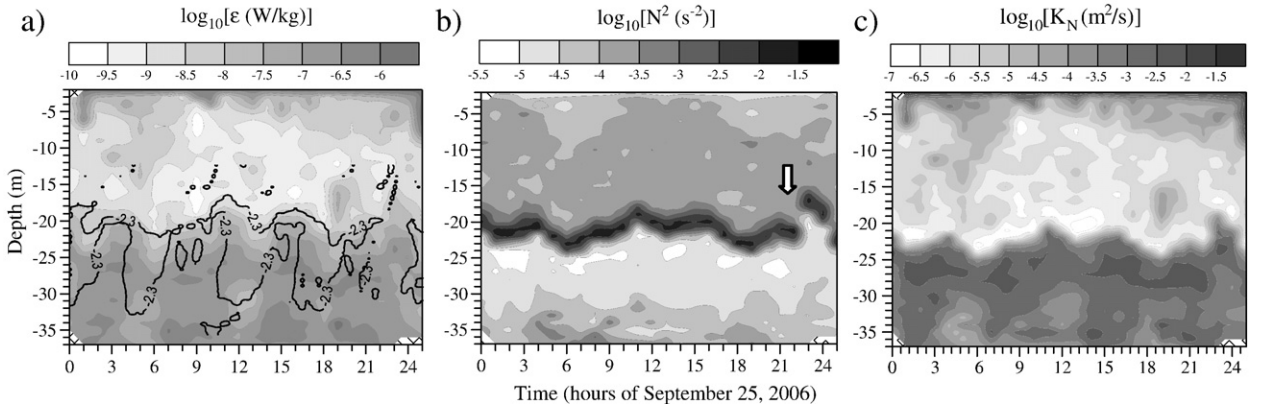

Fig. 9. The time-depth variations of the logarithm of turbulent kinetic energy dissipation rate overlaid by the marked ($\log_{10}[Sh\ (s^{-1})]=-2.3$) contours of shear (a), the squared buoyancy frequency (b), and the eddy diffusivity (c) at **S2**. The arrow in panel (b) points to the pycnocline displacement presumably caused by an internal wave soliton of elevation.

close to the seafloor ($\zeta = 3.9$ mab) whereas the weakest motions were in the vicinity of the pycnocline ($\zeta = 18.9$ mab). This is in agreement with the eigenfunctions of horizontal velocities of linear internal waves (not shown) calculated from the averaged profile of $\hat{N}^2(z)$ shown in Fig. 5b.

In addition to ever-present linear quasi-sinusoidal waves, a sharp and short-lived (~1 h) vertical distortion of the pycnocline was observed around $t = 23$ h (see Fig. 5b), which could be caused by the passage of an internal soliton of elevation with an amplitude of ~4–5 m. Note that the mean depth of the pycnocline was at $z = -20$ m ($\zeta = 18$ mab) and the mean thicknesses of the upper and lower quasi-homogeneous layers were $h_1 = 20$ m and $h_2 = 18$ m, respectively. The observations indicate that traditional soliton of depression of the open sea ($h_2 >> h_1$) can transform to a soliton of elevation ($h_2 < h_1$) near **S2** as it propagates onshore. This soliton, however, was not captured in detail because of the coarse sampling rate of our profiling measurements (1-h bursts of 3 consecutive casts), but the unusual jump up of the whole pycnocline at $t \sim 23$ h and its relaxation to the same depth at $t \sim 24$ h suggest the possibility of its existence.

In contrast to **S1**, the entire layer between the pycnocline and the seafloor at **S2** was completely turbulent. The magnitude of ε therein varied in time but the dissipation was always above 10^{-8} W/kg, increasing up to 10^{-6} W/kg near the seafloor during the periods of maximum tidal magnitudes (Fig. 9a). The influence of tidal periodicity on the generation of near-bottom turbulence is clear from the dissipation and diffusivity plots (Fig. 9a, c). The contours of equal shear below the pycnocline in Fig. 9a ($\log_{10} Sh = -2.3$ [Sh is in s^{-1}]) exhibit inclined zones of alternative increase and decrease of ε suggesting that the BBL turbulence is governed by tidally-induced shear at the bottom, which propagates upwards with a phase speed of 5–6 m/h. This is in agreement with the estimates of shear propagation reported in Lozovatsky et al. (2008a) for a region in YS with approximately the same depth (38 m) as that at **S2**.

Three series of vertical profiles of $Sh^2(\zeta)$, $\varepsilon(\zeta)$, and $Ri(\zeta)$, where $Ri = N^2/Sh^2$ is the gradient Richardson number, are shown in Fig. 11 between the first level of ADCP measurements and the upper boundary of the pycnocline ($\zeta = 3$–20 mab). The ADCP shear was calculated with a 1 m vertical resolution in order to match the ε and N^2 profiles and obtain Ri at the same levels as those of ε and K_N. The Sh^2, ε and Ri at every height varied over an order of magnitude due to the variation of the magnitude of tidal current. In the pycnocline ($\zeta = 15$–20 mab), the range of Ri variation was about 4 decades (see also a wide range of N^2 variability in the pycnocline in Fig. 5b). The profiles in Fig. 11 show two sub-layers below the pycnocline. These are the sheared near-bottom layer ($\zeta < 8$ mab) where both Sh^2 and shear-induced dissipation decrease upwards and an intermediate sub-layer from $\zeta = 8$ mab to the lower boundary of the pycnocline. In the near-bottom sheared layer, the gradient Richardson number, as expected, decreases towards the seafloor and lay below unity most of the time, in particular $Ri < 0.25$ near the bottom. In the intermediate sub-layer, all variables were almost constant with ζ suggesting an equilibrium state. This state was discussed by Strang and Fernando (2001a) where under certain conditions the stratification and shear adjust to achieve the maximum mixing efficiency. In the pycnocline, where the gradient Richardson number was mostly much above critical, the dissipation decreased with height, accompanied by an increase rather than a decrease of shear. This increase of shear is a common feature in stratified flows under $Ri > 1$ conditions. Because of the damping of turbulence, the momentum cannot be vertically transferred and thus the shear tends to increase (Pardyjak et al., 2002). The increase of Sh^2 was also associated with a specific shape of the velocity profile that contained a maximum below the pycnocline.

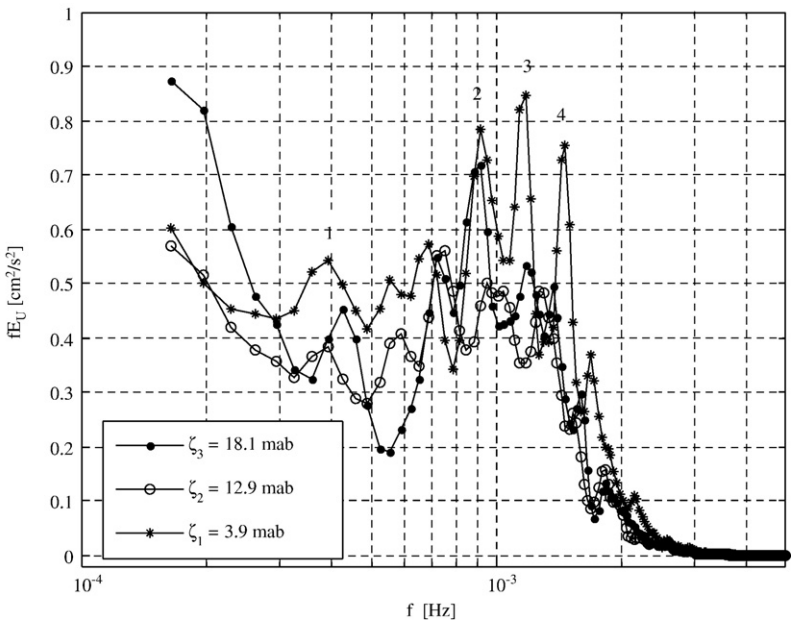

Fig. 10. The energy-preserving spectra fE_U of horizontal tidal residuals at **S2** near the bottom (ζ_1), in (ζ_3) and below (ζ_2) the pycnocline. Several distinct spectral maxima (1–4) indicate internal oscillations of periods ~43, 18, 14, and 11 min, respectively.

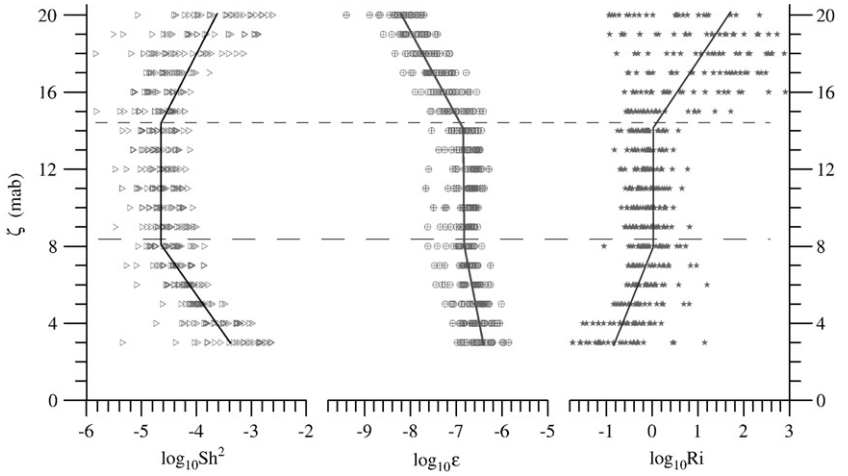

Fig. 11. A series of vertical profiles of the squared shear (left), the dissipation rate (center), and the gradient Richardson number (right) at **S2**. The upper boundary of the near-bottom shear layer ($\zeta = 8$ mab) and the lower boundary of the pycnocline ($\zeta = 15$ mab) are depicted by long and short dashed lines, respectively.

Various mechanisms that can lead to the formation of such vertical structure of tidally-dominated currents in YS were discussed in Lozovatsky et al. (2008a).

A contour plot of the time-depth variation of *Ri* at **S2** (Fig. 12) shows that near the seafloor there is a high potential for shear instability ($Ri < 0.25$) during the high-magnitude phase of tidal currents (approximately 3 h long for each semidiurnal period). Because the bottom-generated shear decreased upwards, the Richardson number increased with ζ, but at all heights from the bottom up to the lower boundary of the pycnocline *Ri* is still below unity. When the magnitude of the tidal current decreases, phases of higher Richardson number emerge (see the light-colored, vertically inclined bands in Fig. 12), lasting approximately the same 3 h as the low-*Ri* phase. The tidal-induced alterations of low and high *Ri* segments in Fig. 12 match well with the corresponding periods of higher and lower dissipation rates in Fig. 9a. These observations support the notion that the generation of turbulence in the entire BBL at **S2** was mainly driven by shear instabilities of tidal currents.

In the pycnocline, where *Ri* was generally high (the light-gray wavy band above $\zeta \sim 15$ mab in Fig. 12), a darker strip of low *Ri* (<1 and even <0.25) can be easily identified at $t = 22$–23 h. This strip of low *Ri* appeared exactly at the same time when a sharp displacement of the pycnocline was observed, presumably due to the passage of a soliton of elevation through the observational site (see Fig. 9b). Although this episode was not captured in detail by profiling data, the ADCP velocities definitely showed a substantial increase of *w* between $t = 22$ and 23 h (Fig. 13). The highest positive vertical velocities were observed at the pycnocline depth, but the influence of the soliton was also detectible near the seafloor in agreement with Diamessis and Redekopp (2006). The tidal-induced variations of the near-bottom pressure P_{btm}, which in

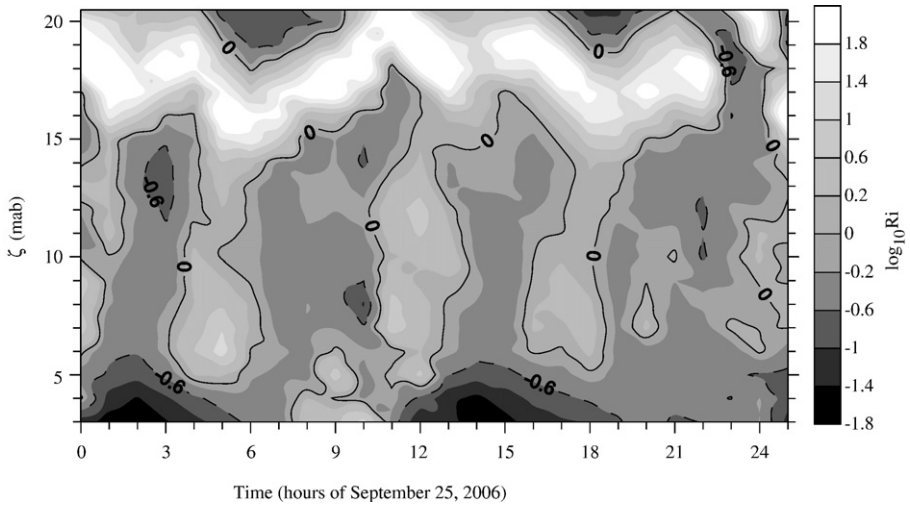

Fig. 12. The logarithm of gradient Richardson number at **S2**. A quarter-diurnal periodicity of the regions with $Ri < 1$ and $Ri > 1$ is highlighted by the isoline $\log_{10}(Ri) = 0$. Note a dark strip of low *Ri* at $t \sim 23$ h above $\zeta > 14$ mab, which "penetrates" the pycnocline (light-colored zone above $\zeta = 15$ mab). This may be due to the instability of an internal wave soliton (see text for details).

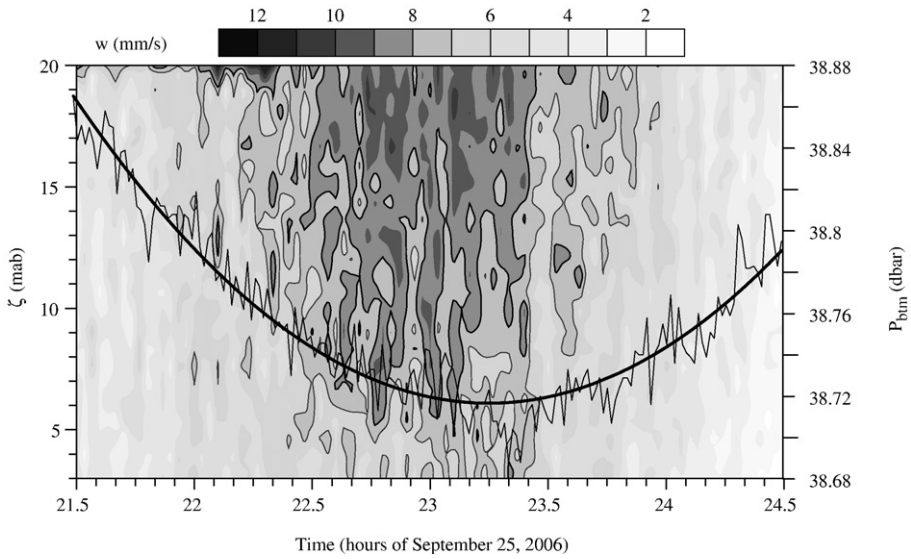

Fig. 13. A contour plot of the vertical ADCP velocity and the variations of bottom pressure P_{btm} (the high-frequency record – thin line; the tidal trend – thick line) during the soliton episode of Fig. 9 ($t = 23$ h).

turn is a measure of the sea surface elevation (see Fig. 13 where a segment of P_{btm} overlays the $w(z,t)$ contour plot), suggest an increase of w and a corresponding lift of the pycnocline during the low tide. The tidal vector of 0.30–0.35 m/s was directed offshore to the east across the isobaths, but direction of the soliton propagation could not be estimated. Lee et al. (2006)

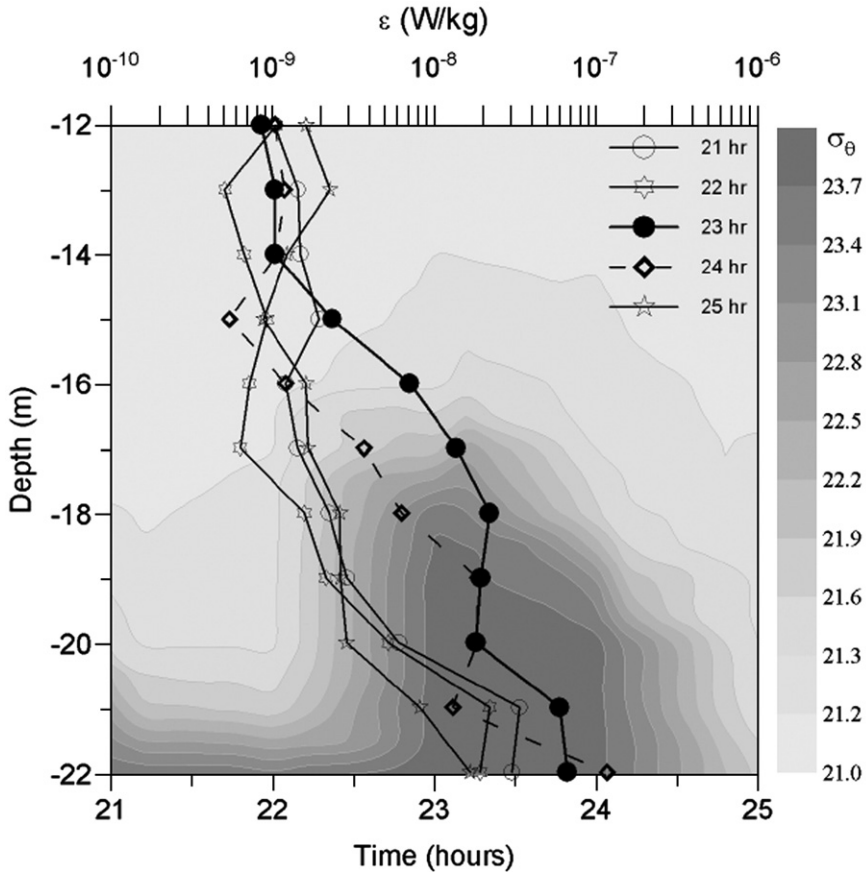

Fig. 14. Hourly profiles of the dissipation rate $\varepsilon(z)$ that included the soliton episode at $t \approx 23$ h at **S2**. The density contour plot of pycnocline displacement between $t \approx 22.5$–24.5 h is given in the background. The depth range containing the pycnocline is chosen to emphasize the event.

reported a series of internal solitons of depression in the East China Sea, specifically associated with the periods of low barotropic tide. The fact that sharp pycnocline distortions described here was also observed during the phase of low tide provides further support for the hypothesis that the passage of an internal soliton of elevation could be responsible for the observed phenomenon. The soliton was accompanied by a significant increase in vertical shear, leading to a low-*Ri* zone across the pycnocline (Fig. 12) and hence to hydrodynamic instabilities and the generation of turbulence. A jump of the dissipation rate by almost an order of magnitude ($\varepsilon \sim 2\times 10^{-8}$ W/kg), which happened at $t=23$ h in the depth range 16–20 m (Fig. 14), suggests that the soliton intensified turbulence in the pycnocline. The turbulent kinetic energy gradually dissipated approximately over 2 h ($\varepsilon \sim (4\text{–}6)\times 10^{-9}$ W/kg at $t=24$ h) to achieve the background level of ε, which was observed prior and after the event (e.g., $\varepsilon \sim (2\text{–}3)\times 10^{-9}$ W/kg at $t=21$, 22, and 25 h). Short observational period of ocean currents and insufficient sampling rate of microstructure measurements limited our analysis on internal waves and turbulence in the region. The issue of soliton generation and their effect on microstructure and waves will be explored in future field experiments.

4. Summary

During a field campaign in the Yellow Sea that included microstructure profiling at two anchored stations in late summer, two distinct regimes of turbulence and mixing were observed. One station was located in the deeper central basin and the other near a shallower local shelf break. The microstructure measurements at the shallower station were augmented by a bottom-mounted ADCP. Weakly stratified surface and bottom boundary layers separated by a narrow pycnocline were observed at the end of the warm season. Under weak winds, the surface-layer turbulence was mainly driven by the diurnal cycle of buoyancy forcing at the sea surface (higher mixing at night and vise versa). In contrast to the wintertime, when the stratification is destroyed by stormy winds and deep convection, thus allowing momentum to transfer over the entire water column (Lozovatsky et al., 2008a), no influence of tidal forcing (tidal shear) was detected in the upper layer of the stratified water column in late summer. On the other hand, the bottom stress due to barotropic tidal currents dominated turbulence near the seafloor. In the deeper (73 m) waters of YS central basin, enhanced rate of dissipation ε and vertical diffusivity K_N were observed up to $\zeta = 10\text{–}15$ mab. At shallower depths (38 m), near a local shelf break, the tidally-induced turbulence completely occupied the lower part of the water column up to the pycnocline ($\zeta \sim 15\text{–}18$ mab). A quarter-diurnal periodicities of ε, with variations in the range $5\times(10^{-8}\text{–}10^{-6})$ W/kg, and K_N ($10^{-5}\text{–}10^{-2}$ m^2/s) were observed at different heights with a time lag of ~5–6 m/h. The gradient Richardson number in the lowest 8 m was below unity 70% of the time, and it was less than 0.25 about 20% of the time, indicating shear instabilities near and above the seafloor.

During the observational period, the deeper-water pycnocline in the central basin was essentially non-turbulent, and no internal-wave activity was detected. As such, vertical fluxes across the pycnocline decreased to molecular levels, retarding the vertical exchange of nutrients and oxygen between the surface and bottom boundary layers that could negatively affect the bio-chemical balance in the region.

On the other hand, internal waves of various periods were observed throughout the whole water column near the local shelf break. Quasi-sinusoidal waves of ~43, 18, 14, and 11 min periods produced distinguished peaks in the energy spectra of horizontal tidal residuals, specifically close to the seafloor. In the pycnocline, turbulence was intermittently preceded by short periods of the decrease of *Ri* probably due to internal wave breaking. A sharp displacement of the pycnocline with amplitude of ~4 m, which was observed during the phase of low tide, was attributed to the passage of an internal solitary wave. The higher thickness of the upper layer compared to the lower layer appears to have created favorable conditions for the generation of a soliton of elevation near the local shelf break. The enhanced shear associated with this internal soliton led to $Ri<0.25$ across the pycnocline, thus enhancing the turbulence to $\varepsilon \sim 2\times 10^{-8}$ W/kg, which is about ten times of the background ε observed before and after the event.

Acknowledgements

The field measurements were funded by the Major State Program of China for Basic Research (grant No. 2006CB400602) and the Program for New Century Excellent Talents in University of China (grant No. NCET-04-0641). The contribution of the third and fourth authors was supported by the US Office of Naval Research (grant N00014-05-1-0245). We wish to thank Dr. Elena Roget (University of Girona, Catalonia, Spain) for useful recommendations and helps in processing the MSS-60 data, and Dr. Daji Huang (the Second Institute of Oceanography, SOA, China) for sharing the CTD data. Comments of two anonymous reviewers and Dr. Hans Burchard, the Guest Editor of this issue, helped to improve the presentation substantially.

References

Alpers, W., He, M.-X., Zeng, K., Guo, L.-F., Li, X.-M., 2005. The distribution of internal waves in the East China Sea and the Yellow Sea studied by multi-sensor satellite images. Proceedings of 2005 International Geoscience and Remote Sensing Symposium, vol. 7. IEEE, pp. 4784–4787.

Baumert, H., Peters, H., 2000. Second-moment closures and length scales for weakly stratified turbulent shear flows. Journal of Geophysical Research 105 (C3), 6453–6468.

Chang, P.-H., Isobe, A., 2003. A numerical study on the Changjiang diluted water in the Yellow and East China Seas. Journal of Geophysical Research 108 (C9), 3299. doi:10.1029/2002JC001749.

Diamessis, P.J., Redekopp, L.G., 2006. Numerical investigation of solitary internal wave-induced global instability in shallow water benthic boundary layers. Journal of Physical Oceanography 36 (5), 784–812.

Dickey, T.D., Williams, A.J., 2001. Interdisciplinary ocean process studies on the New England shelf. Journal of Geophysical Research 106 (C5), 9427–9434.

Egbert, G.D., Ray, R.D., 2000. Significant dissipation of tidal energy in the deep ocean inferred from satellite altimeter data. Nature 405, 775–778.

Fedorov, K.N., 1978. The thermohaline finestructure of the ocean. Pergamon Press, Oxford. 170 pp.

Fringer, O.B., Street, R.L., 2003. The dynamics of breaking progressive interfacial waves. Journal of Fluid Mechanics 494, 319–353.

Holloway, P.E., Chatwin, P.G., Craig, P., 2001. Internal tide observations from the Australian North West Shelf in summer 1995. Journal of Physical Oceanography 31 (5), 1182–1199.

Howarth, M.J., Simpson, J.H., Sündermann, J., van Haren, H., 2002. Processes of Vertical Exchange in Shelf Seas (PROVESS). Journal of Sea Research 47 (3–4), 199–208.

Hsu, M.K., Liu, A.K., Liu, C., 2000. A study of internal waves in the China Seas and Yellow Sea using SAR. Continental Shelf Research 20 (4), 389–410.
Kelley, D.E., Fernando, H.J.S., Gargett, A.E., Tanny, J., Özsoy, E., 2003. The diffusive regime of double-diffusive convection. Progress in Oceanography 56 (3), 461–481.
Kim, S.-C., Friedrichs, C.T., Maa, J.P.-Y., Wright, L.D., 2000. Estimating bottom stress in tidal boundary layer from acoustic Doppler velocimeter data. Journal of Hydraulic Engineering 126 (6), 399–406.
Lee, J.-H., Lozovatsky, I., Jang, S.-T., Jang, C.-J., Hong, C.-S., Fernando, H.J.S., 2006. Episodes of nonlinear internal waves in the Northern East China Sea. Geophysical Research Letters 33 (L18601). doi:10.1029/2006GL027136.
Lie, H.-J., Cho, C.-H., 1994. On the origin of the Tsushima Warm Current. Journal of Geophysical Research 99 (C12), 25,081–25,091.
Liu, Z., Wei, H., 2007. Estimation to the turbulent kinetic energy dissipation rate and bottom shear stress in the tidal bottom boundary layer of the Yellow Sea. Progress in Natural Science 17 (3), 289–297.
Liu, A.K., Chang, Y.S., Hsu, M.-K., Liang, N.K., 1998. Evolution of nonlinear waves in the East and South China Seas. Journal of Geophysical Research 103 (C4), 7995–8008.
Lombardo, C.P., Gregg, M.C., 1989. Similarity scaling of viscous and thermal dissipation in a convecting surface boundary layer. Journal of Geophysical Research 94 (C5), 6273–6284.
Lozovatsky, I.D., Fernando, H.J.S., 2002. Mixing on a shallow shelf of the Black Sea. Journal of Physical Oceanography 32 (3), 945–956.
Lozovatsky, I., Figueroa, M., Roget, E., Fernando, H.J.S., Shapovalov, S., 2005. Observations and scaling of the upper mixed layer in the North Atlantic. Journal of Geophysical Research 110 (C05013). doi:10.1029/2004JC002708.
Lozovatsky, I., Roget, E., Fernando, H.J.S., Figueroa, M., Shapovalov, S., 2006. Sheared turbulence in a weakly-stratified upper ocean. Deep Sea Research I 53 (2), 387–407.
Lozovatsky, I.D., Liu, Z., Wei, H., Fernando, H.J.S., 2008a. Tides and mixing in the northwestern East China Sea. Part I: Rotating and Reversing flows. Continental Shelf Research 28 (2), 318–337.
Lozovatsky, I.D., Liu, Z., Wei, H., Fernando, H.J.S., 2008b. Tides and mixing in the northwestern East China Sea. Part II: Near-bottom turbulence. Continental Shelf Research 28 (2), 338–350.
MacKinnon, J.A., Gregg, M.C., 2003. Mixing on the late-summer New England Shelf—solibores, shear, and stratification. Journal of Physical Oceanography 33 (7), 1476–1492.
Matsuno, T., Lee, J.-S., Shimizu, M., Kim, S.-H., Pang, I.-C., 2006. Measurements of the turbulent energy dissipation rate ε and an evaluation of the dispersion process of the Changjiang Diluted Water in the East China Sea. Journal of Geophysical Research 111 (C11S09). doi:10.1029/2005JC003196.
Nasmyth, P.W., 1970. Oceanic turbulence. PhD dissertation Thesis, University of British Columbia, Vancouver, Canada, 69 pp.
Navrotsky, V.V., Lozovatsky, I.D., Pavlova, E.P., Fernando, H.J.S., 2004. Observations of internal waves and thermocline splitting near a shelf break of the Sea of Japan (East Sea). Continental Shelf Research 24 (12), 1375–1395.
Osborn, T., 1980. Estimates of the local rate of diffusion from dissipation measurements. Journal of Physical Oceanography 10 (1), 83–89.
Panchev, S., Kesich, D., 1969. Energy spepctrum of isotropic turbulence at large wavenumbers. Comptes rendus de l'académie Bulgare des sciences 22, 627–630.
Pardyjak, E.R., Monti, P., Fernando, H.J.S., 2002. Flux Richardson number measurements in stable atmospheric shear flows. Journal of Fluid Mechanics 449, 307–316.
Prandke, H., Stips, A., 1998. Test measurements with an operational microstructure-turbulence profiler: Detection limits of dissipation rates. Aquatic Sciences 60, 191–209.
Qiao, F., Ma, J., Xia, C., Yang, Y., Yuan, Y., 2006. Influence of the surface wave-induced and tidal mixing on vertical temperature structure of the Yellow and East China Seas in summer. Progress in Natural Science 16 (7), 739–746.
Rippeth, T.P., 2005. Mixing in seasonally stratified shelf seas: a shifting paradigm. Philosophical Transactions of the Royal Society A 363, 2837–2854.
Rippeth, T.P., Inall, M.E., 2002. Observations of the internal tide and associated mixing across the Malin Shelf. Journal of Geophysical Research 107 (C4), 3028. doi:10.1029/2000JC000761.
Rippeth, T.P., Fisher, N.R., Simpson, J.H., 2001. The cycle of turbulent dissipation in the presence of tidal straining. Journal of Physical Oceanography 31 (8), 2458–2471.
Rippeth, T.P., Simpson, J.H., Williams, E., Inall, M.E., 2003. Measurement of the rates of production and dissipation of turbulent kinetic energy in an energetic tidal flow: Red Wharf Bay revisited. Journal of Physical Oceanography 33 (9), 1889–1901.
Rippeth, T.P., Palmer, M.R., Simpson, J.H., Fisher, N.R., Sharples, J., 2005. Thermocline mixing in summer stratified continental shelf seas. Geophysical Research Letters 32 (L05602). doi:10.1029/2004GL022104.
Roget, E., Lozovatsky, I., Sanchez, X., Figueroa, M., 2006. Microstructure measurements in natural waters: methodology and applications. Progress in Oceanography 70 (2–4), 126–148.
Sharples, J., Moore, C.M., Abrahams, E.R., 2001. Internal tide dissipation, mixing, and vertical nitrate flux at the shelf edge of NE New Zealand. Journal of Geophysical Research 106 (C7), 14,069–14,081.
Shi, J., Wei, H., 2007. Evidence of double diffusion in the East China Sea. Journal of Marine Systems 67 (3–4), 272–281.
Simpson, J.H., Crawford, W.R., Rippeth, T.P., Cambell, A.R., Cheok, J.V.S., 1996. The vertical structure of turbulent dissipation in shelf seas. Journal of Physical Oceanography 26 (8), 1579–1590.
Stips, A., 2005. Dissipation measurements: theory. In: Baumert, H., Simpson, J.H., Suendermann, J. (Eds.), Marine turbulence: theories, observations and methods. Cambridge University Press, Cambridge, pp. 115–126.
Stips, A., Prandke, H., 2000. Recommended algorithm for dissipation rate calculation within PROVESS. PROVESS Report. 17 pp.
Strang, E.J., Fernando, H.J.S., 2001a. Vertical mixing and transports through a stratified shear layer. Journal of Physical Oceanography 31 (8), 2026–2048.
Strang, E.J., Fernando, H.J.S., 2001b. Entrainment and mixing in stratified shear flows. Journal of Fluid Mechanics 428, 349–386.
Thorpe, S.A., 2005. The turbulent ocean. Cambridge University Press, Cambridge. 485 pp.
Turner, J.C., 1979. Buoyancy effects in fluids. Cambridge University Press, Cambridge. 368 pp.
van Haren, H., 2000. Properties of vertical current shear across stratification in the North Sea. Journal of Marine Research 58, 465–491.
van Haren, H., Mass, L., Zimmerman, J.T.F., Ridderinkhof, H., Malschaert, H., 1999. Strong inertial currents and marginal internal wave stability in the central North Sea. Geophysical Research Letters 26 (19), 2993–2996.
Wolk, F., Yamazaki, H., Seuront, L., Lueck, R.G., 2002. A new free-fall profiler for measuring biophysical microstructure. Journal of Atmospheric and Oceanic Technology 19 (5), 780–793.